ROYAL SOCIETY
OF CHEMISTRY

PAPER

Check for updates

Origins of electrical conductivity in 3D iron-tetrazole-based metal–organic frameworks

María Esteve-Rochina, [ID] [a] Jennifer Faro-Guara,[a] Enrique Ortí, [ID] [a] Aron Walsh [ID] [b]
and Joaquín Calbo [ID] *[a]

Electrically conductive metal–organic frameworks (MOFs) have emerged as materials for energy conversion and storage, with the advantages of intrinsic porosity and high tunability. One promising strategy to design conducting MOFs is the use of electroactive ligands, combined with mixed-valence phenomena promoted by redox-accessible inorganic pairs. In this regard, a porous material based on a nitrogenated ligand (benzeneditetrazole, BDT) and the transition metal cation Fe(II), $Fe_2(BDT)_3$, holds a record conductivity among 3D MOFs. Its efficient charge transport was ascribed to the $-(Fe-N-N-)_\infty$ network, opening the door to the design of novel conducting materials based on that scaffold. We present a theoretical investigation of the charge-transport properties for the record $Fe_2(BDT)_3$ polymorph, and extend the study to two analogous polymorphs with the same chemical composition but different crystal symmetry. Density functional theory calculations of the electronic band structure reveal the presence of alternative transport channels with high electronic delocalization along the π-conjugated ditetrazole ligand in combination to the iron–nitrogen chain. Our results demonstrate that ligand protonation distribution mandates charge-transport efficiency, and defines a different hole/electron conduction pathway for each polymorph. We thus propose a new strategy to enhance conductivity in porous materials based on protic ligands through engineering of protonic ordering. A detailed analysis of the partial Fe(II) oxidation to Fe(III) confirms insertion of empty Fe(III)-d energy levels within the bandgap with a small energy penalty, thus allowing enhancement of the electronic properties of the material through mixed-valence phenomena. This work provides insights into the factors influencing charge transport in MOFs, guiding the design and discovery of advanced porous conductors for next-generation applications.

Introduction

Metal–organic frameworks (MOFs) are crystalline porous materials built from organic ligands and metal nodes. These materials have experienced a growing interest in the last decade due to their extraordinary chemical structure versatility and inherent porosity.[1] Since their discovery,[2,3] MOFs have been used in a wide range of applications such as sensing,[4] catalysis,[5] gas separation and storage.[6] However, the exploitation of porous frameworks in next-generation applications for energy storage and conversion has traditionally been hampered by the insulating nature of their constituting building blocks, namely closed-shell metal nodes and redox-inactive ligands.[7,8] Nowadays, there are several approaches to boost electrical conductivity in MOFs based on their components: (i) presence of redox-active inorganic clusters, (ii) insertion of electroactive organic ligands, and (iii) inclusion of redox-active guests in the framework, either covalently or through noncovalent

interactions. In the inorganic cluster approach, metal ions act as coordination centres to the organic ligands and can be oxidized or reduced, providing electrons that can move through the framework, thus promoting electrical conductivity in the MOF. One of the most common inorganic clusters is based on transition metals such as iron, which has great potential as an electroactivator due to its ability to coexist in multiple oxidation states (*i.e.*, Fe(II)/Fe(III)), leading to mixed valence. Electroactivation through a ligand approach, on the other hand, consists in the use of electron-donor or electron-acceptor organic ligands such as tetrathiafulvalene,[9–11] perylene[12–14] or benzeneditetrazole.[15,16] These ligands are coordinated to the metal ions and, depending on the metal, can exist in different stable oxidation states. The third electroactivation strategy implies the incorporation of a molecule that can either give or accept electrons to/from the framework (*e.g.*, iodine,[12,17–20] tetracyanoquinodimethane,[21–23] *etc.*) *via* redox reactions. This molecule (known as a guest) interacts either with the metal ions or with the organic ligands, generating free charge carriers for efficient conductivity.

Most recent advances in the field of porous conductors are accomplished for low-dimensional MOFs, which can benefit

[a] *Instituto de Ciencia Molecular (ICMol), Universitat de València, Paterna 46980, Spain. E-mail: joaquin.calbo@uv.es*

[b] *Department of Materials, Imperial College London, London SW7 2AZ, UK*

19026 | *J. Mater. Chem. C*, 2025, **13**, 19026–19036

This journal is © The Royal Society of Chemistry 2025

from fully π-d conjugated paths in a 1D channel (1D-MOFs) or a 2D plane (2D-MOFs), thus enabling efficient charge transport through highly delocalized polarons (band transport), even in the presence of hydrogenic defects.[24] For example, conductivities as large as 156.7 S cm^{-1} were reported for Ni-MOF-1D.[25] For layered 2D-MOFs, impressive mobilities up to 220 and 99(hole)/116(electron) cm^2 V^{-1} s^{-1} have been recorded for Fe$_3$(THT)$_2$(NH$_4$)$_3$ and Cu$_3$(BHT), respectively.[26,27] In contrast, 3D frameworks stand behind in terms of charge-transport properties, one of the maximum conductivities (0.3(1) S cm^{-1}) being recorded for Fe(tri)$_2$(BF$_4$)$_{0.33}$ at room temperature.[28] Nonetheless, three-dimensional MOFs possess the advantage of displaying a robust platform in the three directions of space, thereby enhancing their structural stability and porosity pattern integrity.[29] These characteristics are key for their use as photo/electro-catalytic sieves, chemiresistive sensors, thermoelectric devices or supercapacitors.

Out of the several electrically conducting MOFs reported up to date, iron(II)-based MOFs are promising materials as their transport properties can be enhanced due to mixed valence—up to 5 orders of magnitude with respect to other divalent transition metals.[30] Particularly, the combination of Fe(II) and the 5,5′-(1,4-phenylene)bis(1H-tetrazole) (H$_2$BDT) ligand leads to the formation of a three-dimensional framework known as Fe$_2$(BDT)$_3$. The Fe$_2$(BDT)$_3$ MOF exhibits polymorphism, adopting different structures depending on the synthesis conditions. Yan and co-workers reported up to three different polymorphs, which differ in their crystalline structure, pore size and magnetic properties.[31,32] Moreover, due to the presence of Fe(II) d^6 ions, one of the polymorphs exhibits spin-crossover phenomena as a response to temperature and pressure.[33-35]

According to Xie and collaborators,[36] the Cmmm Fe$_2$(BDT)$_3$ polymorph (named here **P3**), displays conductivity values from 10^{-5} S cm^{-1} (just after its synthesis), to 0.3 S cm^{-1} (after 7-day air exposure), to 1.2 S cm^{-1} (after 30-day air exposure) and to a maximum value of 1.8 S cm^{-1}, being the later the highest conductivity value reported for a 3D MOF up to date. In that work, the material was demonstrated to undergo partial oxidation due to atmospheric oxygen, leading to mixed-valence Fe(II)/Fe(III) states.[36,37] The high charge mobility in the porous framework was attributed to the –(Fe–N–N–)$_\infty$ chains,[36] yet the electronic band structure suggests alternative ligand-centred pathways that may be relevant for carrier transport. Moreover, the formation of a mixed-valence Fe(II)/Fe(III) promotes the presence of unoccupied states within the bandgap, thus enhancing the conducting properties of the material.[36,37] Despite being built from the same building blocks as **P3**, and thus presumably constituting promising candidates for charge conduction, the analogous Fe$_2$(BDT)$_3$ polymorphs (here **P1** and **P2**) have not been studied for this purpose thus far.

Herein, we present a comprehensive theoretical characterization by means of quantum chemical calculations to unveil the origin of the high charge-transport properties of the Fe$_2$(BDT)$_3$ **P3** polymorph, and extend the analysis to the analogous **P1** and **P2** polymorphs as promising porous materials for conduction. The crystal and electronic structure of the Fe$_2$(BDT) polymorphs have been characterized using hybrid density functional theory.

Our *ab initio* calculations indicate the presence of alternative transport channels to the –(Fe–N–N–)$_\infty$ network, which display high electronic delocalization that extends longitudinally through the π-conjugated tetrazole ligands, and originate from protonated/deprotonated ligand distribution along the three axes. The effect of the protonic ordering in the charge transport properties, particularly bandgap and charge carrier effective masses, has been thoroughly investigated. Finally, we study in detail the effect of partial Fe(II) oxidation in generating empty energy levels within the bandgap, and its implications in enhancing the conducting properties of the porous materials.

Methodology

Molecular calculations and crystal structure calculations using periodic boundary conditions were carried out at the density functional theory (DFT) level using the all-electron FHI-aims program suite.[38-40] The minimum-energy structure of the organic ligand in the different protonation states and of the three different polymorphs of Fe$_2$(BDT)$_3$ were first obtained after full lattice and ionic relaxation by using the Broyden–Fletcher–Goldfarb–Shanno optimization algorithm,[41] employing the tier-1 numerical atom-centered orbital (NAO) basis set in "intermediate" species settings, and the gradient generalized approximation through the PBEsol functional.[42] In the case of the molecular calculations, further optimization was performed by using the screened-hybrid HSE06 functional.[43] The screening parameter of HSE06 was set to 0.11 Bohr^{-1}. In the periodic calculations of **P1–P3**, conventional cells were used to explore the reciprocal space during crystal optimization (k-grid of 1 × 1 × 1). The choice of the k-grid was based on convergence tests to maximize accuracy-cost ratio (see Table S1). Relativistic effects were included with the atomic, scalar, zero-order regular approximation as implemented in FHI-aims.[44]

Starting from the original crystal structure of **P2**, potential protonation sites were identified on the tetrazole ligands, specifically at the nitrogen atoms known for being protonated. Random protonation configurations were then generated by assigning protons to these sites in an arbitrary yet chemically coherent manner, while preserving the overall stoichiometry and electroneutrality of the system. Up to three random configurations were generated for **P2**. The electronic structures of these configurations are qualitatively equivalent, with small variations in bandgap values (<0.2 eV). We therefore selected one of them for subsequent analyses.

Convergence criteria for the self-consistent field cycles were set to a charge density below 1 × 10^{-6} eV, while the threshold for structural relaxation was chosen at forces lower than 10^{-2} eV per Å per atom. Single-point band structure calculations were performed at the HSE06 functional with a k-grid of 3 × 3 × 3 for **P1–P3**. This method provides a more reliable and general description of strongly correlated d-electron systems (as in the iron-based Fe$_2$(BDT)$_3$ polymorphs) compared to e.g. the DFT+U scheme, which requires semi-empirical tuning of the Hubbard U parameter.[45]

This journal is © The Royal Society of Chemistry 2025

J. Mater. Chem. C, 2025, **13**, 19026–19036 | **19027**

For low-spin $Fe_2(BDT)_3$ polymorphs, the total spin was set to zero, and spin-restricted (unpolarized) calculations were performed. On the other hand, for high-spin and mixed-valence $Fe_2(BDT)_3$ systems, spin-polarized (collinear) calculations were carried out. **P2′** was modelled by taking the optimized **P2** structure and placing H_2BDT along one of the equivalent directions in the *ab* plane, while BDT^{2-} ligands were aligned along the remaining two directions, resulting in an ordered protonic distribution. **P3′** was modelled by taking the optimized **P3** structure and then placing randomly the H_2BDT and BDT^{2-} ligands, in such a way that the chemical formula $Fe_2(H_{0.67}BDT)_3$ was fulfilled. In this case, a $1 \times 1 \times 2$ supercell was generated to allow random protonic distribution of **P3′**. Regarding mixed-valence **P2** and **P3**, each structure was represented with 50% Fe(III) atoms in both high-spin (HS) and low-spin (LS) configurations, and 50% Fe(II) atoms in the LS configuration. Mixed-valence **P1**, on the other hand, was modelled with 50% Fe(III) atoms in both high-spin (HS) and low-spin (LS) configurations, and 50% Fe(II) atoms in the HS configuration.

The electronic level alignment to the vacuum was done by considering the Hartree potential of each system within the pore. First, the Hartree potential was computed using the FHI-aims package with the hybrid HSE06 functional. Then, the electronic levels were aligned to the vacuum level according to the protocol implemented in the Macrodensity package,[46] consisting on the computation of the spherical average of the electrostatic potential at the pore centre.

The effective mass is an important quantity that relates with the charge transport properties of a material through the definition of the charge carrier mobility μ:

$$\mu = \frac{q\tau}{m^*}$$

where q is the elementary charge of the carrier, τ is the mean relaxation time between collisions and m^* is the effective mass associated to the carrier. The effective mass is conventionally defined as:

$$m^* = \hbar^2 \left(\frac{\delta^2 E}{\delta k^2} \right)^{-1}$$

where E is the electronic band energy at wavevector k, and describes the acceleration that a charge carrier experiments upon electric field application. This definition is formally valid for parabolic bands, and provides a basis for the description of charge transport in semiconductors.[47] However, metal–organic frameworks usually display non- or weakly parabolic bands, and hence the definition of the effective mass is modified to obtain a proper description of the non-quadratic curvature of the band.[47] In the effmass package,[48] this is done by either (i) incorporating higher order energy terms in the dispersion relation (obtaining the transport effective mass) or (ii) considering the occupation of all bands as determined by the Fermi–Dirac distribution (optical effective mass). The Kane quasi-linear dispersion approximation is based on the first approach by keeping only the first nonlinear term, thus obtaining an effective mass described by two parameters: the transport effective mass at the band edge ($m_{t,0}$) and the α parameter, which quantifies the amount of non-parabolicity:

$$m^\star = m_{t,0}(1 + 2\alpha E)$$

In this work, effective masses were computed using the Kane approximation as implemented in the effmass package.[48]

Crystal structure geometries, frontier crystal orbitals and spin densities were displayed with the VESTA visualization software,[49] while molecular structures and the corresponding frontier molecular orbitals were displayed with the help of the Chemcraft software.[50] The projected density of states was plotted with a Gaussian broadening of 0.1 eV.

Results and discussion

Molecular organic ligand

$Fe_2(H_{0.67}BDT)_3$ is a family of metal–organic frameworks (hereafter abbreviated as $Fe_2(BDT)_3$) based on the benzeneditetrazole ligand 5,5′-(1,4-phenylene)bis(1*H*-tetrazole) (H_2BDT), whose heterorings can be presented either protonated or deprotonated depending on the ligand position in a particular polymorph. Therefore, prior to studying and analysing the structural and electronic properties of $Fe_2(BDT)_3$ crystals, the characteristics of the constituting bidentate tetrazole ligand BDT in its different protonation forms were examined.

The electroactive character of the BDT ligand stems from the nitrogen atoms of the tetrazole rings and its protonation state. The electron lone pairs of the electronegative nitrogen atoms enable the coordination bonding to a metallic node as in the $Fe_2(BDT)_3$ family of MOFs. Consequently, tetrazole rings may act as electron donors. On the other hand, BDT may also act as an electron acceptor by accommodating the electronic density excess along the π-conjugated system formed by the two tetrazole rings and the central benzene ring.

Molecular calculations on the protonated (H_2BDT) and deprotonated ($HBDT^-$ and BDT^{2-}) forms of the benzeneditetrazole ligand were performed at the hybrid HSE06/tier-1 NAO level of theory. Theoretical calculations predict that the energy required to extract one proton from the H_2BDT ligand, leading to the $HBDT^-$ species, is of 14.01 eV. Extraction of a second proton to form BDT^{2-} costs 16.73 eV. These penalties are expected to decrease when the ligand interacts coordinatively with Fe(II) in forming $Fe_2(BDT)_3$. As a reference, the deprotonation energy of imidazole and tetrazole molecules at the same level of theory are 15.59 and 14.69 eV, respectively, indicating an easier first deprotonation as the number of nitrogens in the azole ring increases and in passing to BDT due to its extended π-conjugation. In terms of energy levels, deprotonation of the BDT ligand not only destabilizes the π/π* frontier highest-occupied and lowest-unoccupied molecular orbitals (HOMO and LUMO, respectively), but also alters their topology (Fig. 1). In going from H_2BDT to $HBDT^-$, there is a decrease in the HOMO–LUMO gap from 4.31 to 3.32 eV, which is accompanied by an asymmetric shift of the electron density. In $HBDT^-$ the HOMO is centred on the deprotonated tetrazole, indicative of its donor character,

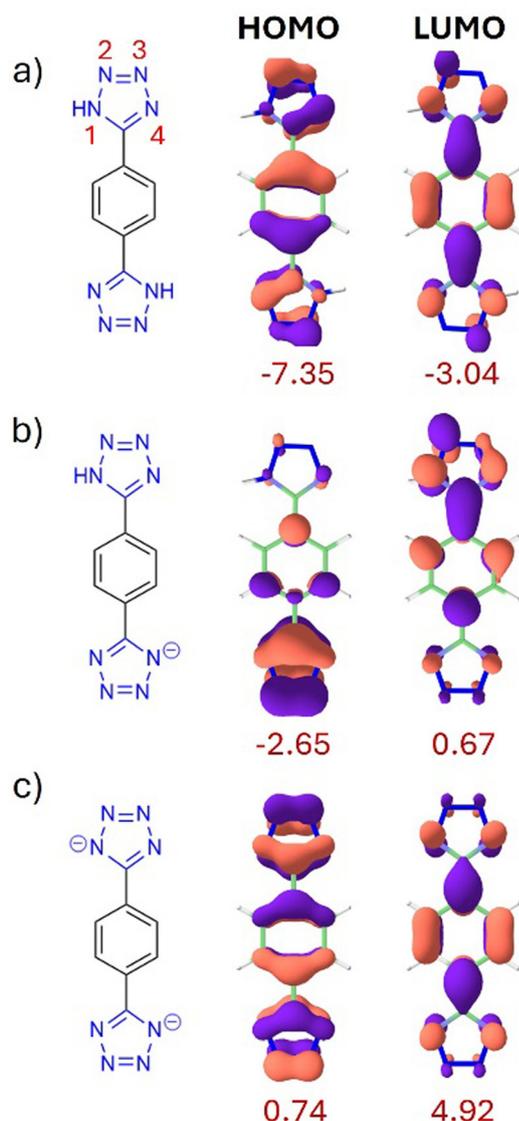Fig. 1 Lewis chemical structures and frontier molecular orbitals (isovalue of 0.05 Bohr^{-3}) calculated at the HSE06/tier-1 intermediate NAO level for: (a) H_2BDT, (b) $HBDT^-$ and (c) BDT^{2-}. The energy of the frontier orbitals is indicated in eV.

and the LUMO spreads over the electron-accepting protonated heterocycle (Fig. 1). After the second deprotonation, the HOMO–LUMO gap increases back to 4.18 eV, and the frontier orbitals spread again along the entire molecule with a topology similar to those of H_2BDT.

To analyse the oxidizing/reducing character of the BDT ligand, Koopman's theorem was applied.[51] The electron affinity was predicted to be 3.04, −0.67 and −4.92 eV for H_2BDT, $HBDT^-$ and BDT^{2-}, respectively. The neutral ligand H_2BDT is thus a good electron acceptor, while insertion of electron density in deprotonated negatively charged ligands is hindered. On the other hand, the ionization potential was calculated to be 7.35, 2.65 and −0.74 eV for H_2BDT, $HBDT^-$ and BDT^{2-}, respectively. Therefore, the electron-donating character of the ligands increases as

deprotonation occurs, reaching a slightly negative IP value (spontaneous oxidation) for BDT^{2-}. These results confirm the dual electron donor/acceptor character of BDT depending on its environment and protonation state.

Crystal structure and spin configuration

Three different porous materials are reported with the $Fe_2(BDT)_3$ chemical composition but with different crystal symmetry (Fig. 2). Polymorph **P1** displays an orthorhombic *Fddd* space group, where the fully deprotonated BDT^{2-} ligands are aligned to the *b* axis and are coordinated to Fe(II) nodes through the outer N atoms (positions 2 and 3 of each tetrazole), whereas the *bc*-diagonal ligands are partially protonated and coordinate laterally through nitrogens 3 and 4 (Fig. 1a). On the other hand, polymorph **P2** presents a trigonal $R\bar{3}m$ symmetry, where BDT ligands form a three-dimensional framework with Fe(II) centers with a random protonic distribution (Fig. 2) that fulfills chemical stoichiometry and electroneutrality. Finally, polymorph **P3**, the record conducting 3D MOF, possesses an orthorhombic *Cmmm* space group, where Fe(II) nodes are linked in two inequivalent directions. In this polymorph, fully protonated H_2BDT ligands align with the *b* axis, while fully deprotonated BDT^{2-} ligands are oriented through the *c* direction (Fig. 2). Interestingly, the deprotonated ligands in **P3** present a significant curvature with a calculated maximum depth of 1 Å. Due to symmetry reduction upon considering discrete protonic distributions in the polymorphs, we used the Brillouin zone of the corresponding lattice system to explore the electronic structure of the materials, *i.e.*, orthorhombic for **P1** and **P3**, and hexagonal for **P2**.

The $Fe_2(BDT)_3$ family of polymorphs contains Fe(II) atoms that are hexa-coordinated to the nitrogen atoms of benzeneditetrazole ligands in an octahedral environment. Depending on the crystal-field splitting caused by the BDT ligands (Δ_o), the Fe(II) electronic configuration can be described by either 6 paired electrons (low-spin configuration, LS) or 4 unpaired electrons (high-spin configuration, HS) (Fig. 3a). Additionally, in the HS configuration, the spin moments of neighbouring atoms along the infinite –$(Fe-N-N-)_\infty$ chains can align in parallel, resulting in ferromagnetic ordering (FM), or antiparallel, leading to an antiferromagnetic arrangement (AFM) (Fig. 3b). Besides magnetic susceptibility experimental measurements, spin configuration can be evaluated by high-level electronic structure calculations[52–54] or more simply by analyzing the Fe–N coordination distances: high-spin states tend to have more electrons in antibonding orbitals compared to low-spin states, resulting in weaker bonds and longer bond distances for the HS configurations.[55]

The crystal structure of the three $Fe_2(BDT)_3$ polymorphs was obtained after full atomic and lattice relaxation at the DFT-PBEsol level of theory and tier-1 NAO intermediate basis set, starting from the single-crystal X-ray data (see Methodology section for further details). The theoretical cell parameters are in good accordance with those obtained experimentally (Table S2).[31] Inclusion of van der Waals (vdW) corrections using the Hirshfeld dispersion scheme by Tkatchenko and Scheffler[56] did not improve the structural description of the polymorphs (Table S2) and was therefore omitted.
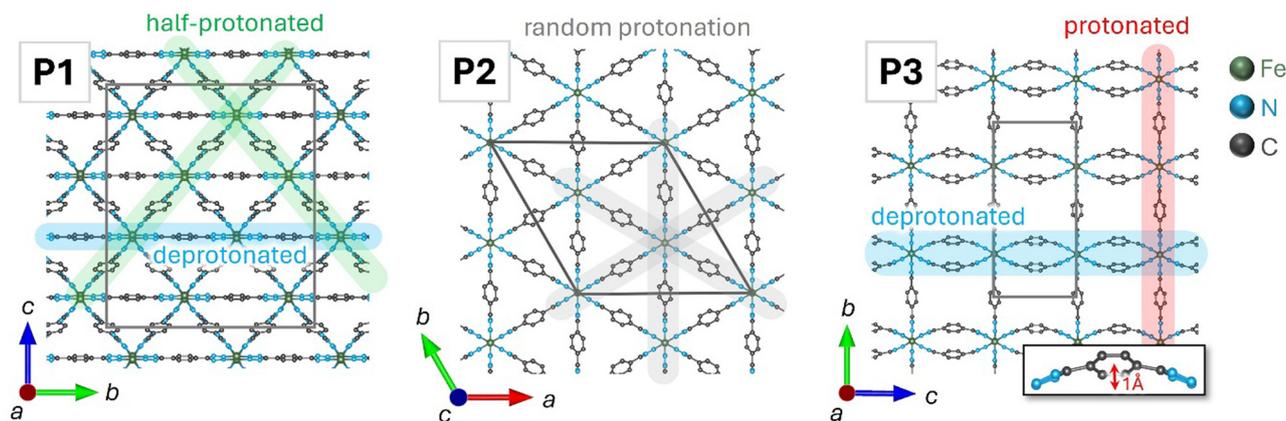
Fig. 2 Optimized crystal structures for the three polymorphs of $Fe_2(BDT)_3$: **P1**, **P2** and **P3**. Fully protonated, half-protonated, fully deprotonated, and randomly protonated ligand directions are highlighted in red, green, blue and grey, respectively. Hydrogen atoms are hidden for clarity.
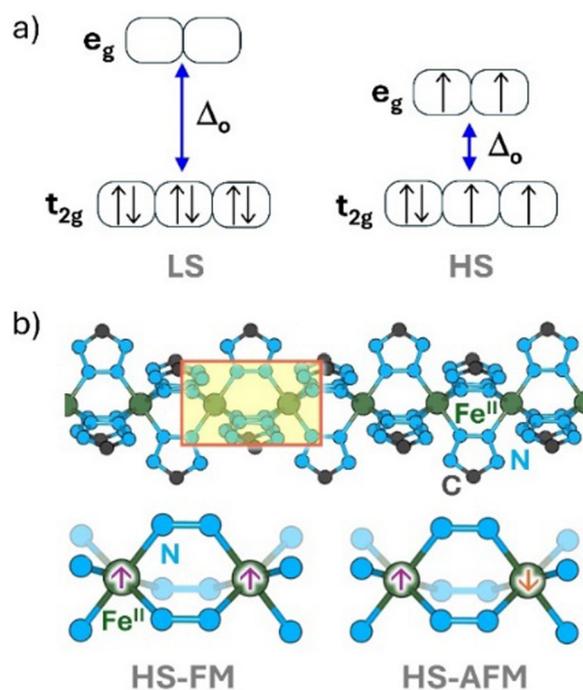

Fig. 3 (a) Crystal-field splitting of the d-orbitals in Fe^{2+} for a low-spin (LS) and high-spin (HS) configuration. Δ_o denotes the crystal-field splitting parameter for an octahedral environment, whereas t_{2g} and e_g are the three lower-energy and two higher-energy degenerate d-orbitals, respectively. (b) Schematic diagram of the metallic node of $Fe_2(BDT)_3$ in a high-spin ferromagnetic (HS-FM) and a high-spin antiferromagnetic (HS-AFM) configuration.

For **P1**, the high-spin FM alignment is favored by 0.82 eV f.u.$^{-1}$ in comparison to the LS configuration (Table S3), which is in line with that found experimentally.[31] The Fe–N bond distances are calculated to be 2.156–2.240 Å, in agreement with the experimental data (2.156–2.248 Å), which further supports a HS configuration for this polymorph.[31] Regarding **P2**, the LS configuration is favored by 0.15 eV f.u.$^{-1}$ with respect to the HS-FM configuration (Table S3). Experimentally, **P2** displays two inequivalent Fe–N coordination environments, with bond distances of 2.172 and

1.963 Å, which are indicative of coexistence of HS and LS states, respectively, at room temperature.[31] Actually, spin-crossover (SCO) phenomena in this polymorph was reported upon cooling. Theoretical calculations indicate that the HS-AFM configuration of **P2** is 0.98 eV f.u.$^{-1}$ less stable than the LS configuration, in good accord with the prevalence of a low-spin state at low temperature. Our calculations do not consider temperature corrections and SCO is not further analyzed. Finally, the low-spin state is the most stable configuration in **P3** (Table S3). Fe–N distances in this state are calculated with average values between 1.871 Å and 1.920 Å, slightly lower than those reported by Yan and coworkers[31] (1.953–1.968 Å), but supporting the modelled spin configuration for **P3**. The HS-AFM configuration in this polymorph converges to a LS wavefunction (Fig. S1), whereas the HS-FM configuration is predicted 0.31 eV f.u.$^{-1}$ less stable than the LS state, with average Fe–N distances of 2.124 Å.

Band structure and conducting properties

To shed light on the electroactive and conducting properties of $Fe_2(BDT)_3$ porous materials, electronic structure calculations were performed at the hybrid DFT level of theory (HSE06/tier-1 NAO) for polymorphs **P1**, **P2** and **P3** in their most stable spin configurations: **P1** (HS-FM), **P2** (LS) and **P3** (LS); **P1** (LS) was also calculated for the sake of comparison. Theoretical calculations predict direct bandgaps centred at Γ of 3.52(α)/2.18(β), 3.17, 2.27 eV and 1.94 eV for **P1** (HS-FM), **P1** (LS), **P2** (LS) and **P3** (LS), respectively (Fig. 4 and Fig. S2). These values indicate that the three polymorphs are relatively low-bandgap materials and have potential to promote VB $\rightarrow$ CB electronic transitions, hence engendering charge carriers for efficient transport. Despite having the same chemical composition, significant differences in the electronic band structure are found, which might stem from the distribution of protonated/deprotonated ligands in the 3D framework, the organic coordination linkage, or the presence of curved *vs.* flat BDT ligands (Fig. 3); *vide infra*.

The electronic band structure of **P1** in its high-spin ferromagnetic configuration (Fig. 4) displays large dispersion in the valence band of the β-channel across electron-donor BDT^{2-}

19030 | *J. Mater. Chem. C*, 2025, **13**, 19026–19036

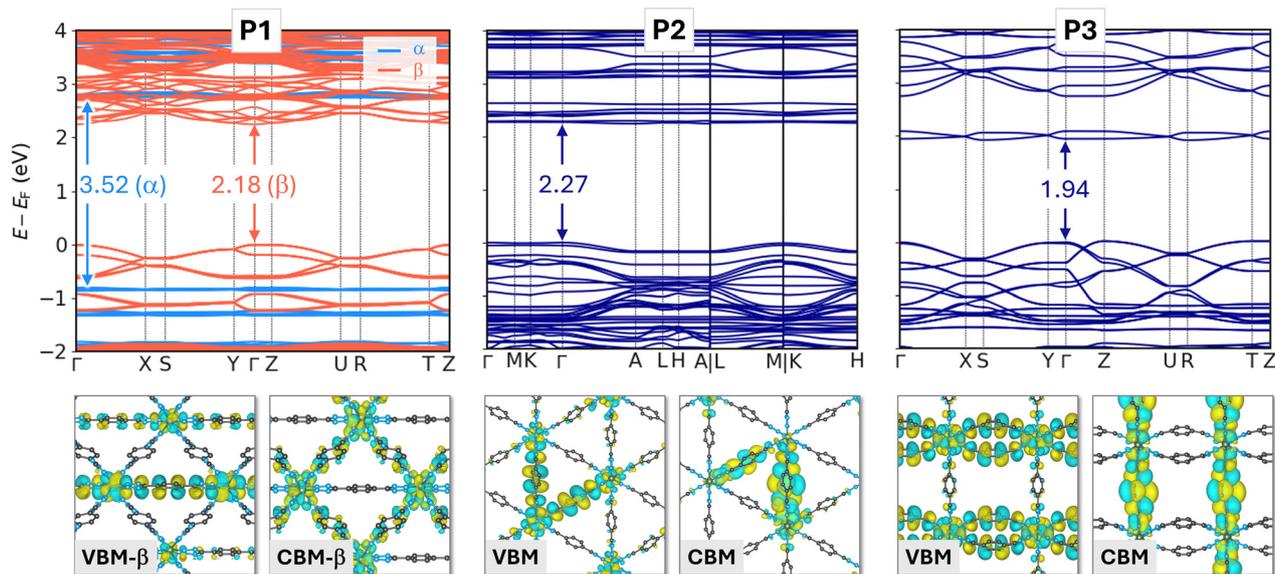This journal is © The Royal Society of Chemistry 2025

Fig. 4 Electronic band structure and frontier crystal orbitals calculated for **P1** (HS-FM), **P2** (LS) and **P3** (LS) at DFT/HSE06. The Fermi level is set to zero at the top of the valence band. VBM and CBM stand for valence-band maximum and conduction-band minimum, respectively. The bandgap value (in eV) is indicated for each band structure.

Table 1 Effective masses for hole (m_h^*) and electron (m_e^*) charge carriers of each polymorph in the most characteristics directions (through ligands and through the Fe–N chain) expressed in free electron mass units $(m_0)^a$

Structure	m_h^*			m_e^*		
	BDT^{2-}	H_2BDT or $HBDT^-$	$-(Fe-N-N-)_\infty$	BDT^{2-}	H_2BDT or $HBDT^-$	$-(Fe-N-N-)_\infty$
P1 (HS)	0.58	1.00	2.06	1.79	1.54	1.53
P1 (LS)	0.42	0.72	1.76	>10	6.69	>10
P2^b	2.34		2.20	2.92		>10
P2′	0.61	1.67	1.92	2.95	0.50	3.49
P3	0.36	3.63	1.40	>10	0.74	>10
P3′^{c}	0.69	2.00	1.71	>10	>10	2.96

^{a} Flat bands with effective mass values larger than 10 m_0 is indicated as >10. ^{b} In **P2**, all ligand directions are equivalent due to symmetry. ^{c} In **P3′**, ligand directions no longer correspond to BDT^{2-} or $H_2BDT/HBDT^-$ nature due to random protonic distribution.

$(\Gamma-Y)$ direction and a moderate dispersion through the $-(Fe-N-N-)_\infty$ chains $(\Gamma-X)$, with hole effective masses (m_h^*) of 0.58 and 2.06 m_0, respectively (Table 1). Otherwise, the conduction band presents large dispersion through the half-protonated (electron-acceptor) $HBDT^-$ and $-(Fe-N-N-)_\infty$ chain directions, with m_e^* of 1.54 and 1.53 m_0, respectively (Table 1). As small effective masses (usually < 1 m_0) are related to efficient conducting properties, this makes **P1** a good conductor for hole carriers, whereas electron transport is expected to be moderate. The corresponding density of states (DOS) indicates the predominance of Fe(II) atoms in the valence band, accompanied by small contributions of C and N atoms of the organic ligand (Fig. S3). In contrast, the conduction band displays a mixed nature of BDT and Fe(II). The crystal orbital corresponding to the valence-band maximum (VBM) is highly delocalized over the Fe–N chain and deprotonated ligands (a and b directions, respectively) (Fig. 4). This delocalization supports the small m_h^* values predicted along $\Gamma-X$ and $\Gamma-Y$

k-segments. Note that a small m_h^* of 1.00 m_0 is also predicted along the bc diagonal ($HBDT^-$ direction) due to the strong dispersion through b (Table 1). Otherwise, the lowest-unoccupied crystal orbital corresponding to the conduction-band minimum (CBM) spreads over the $HBDT^-$ ligands and Fe(II) (Fig. 4). As the distribution of the half-protonated $HBDT^-$ ligands is random in this polymorph, the delocalization in the CBM is less efficient through ligands, thus providing generally larger values for m_e^* (Table 1).

Regarding **P1** in its low-spin configuration, the band structure is predicted again with large dispersion in the valence band through BDT^{2-} and $-(Fe-N-N-)_\infty$ chain directions (Table 1), with m_h^* of 0.42 and 1.76 m_0, respectively. However, in contrast to **P1** (HS-FM), the effective masses calculated for **P1** (LS) along the conduction band are found significantly larger (>6 m_0). In this case, the frontier crystal orbital associated to the CBM is fully localized over the BDT ligands, with negligible participation of Fe(II) as its empty d-orbitals are placed higher in energy

(Fig. S2 and S3). These results suggest that transport of electrons is significantly improved in the high-spin state of **P1**, promoted by a mixed nature of the conduction band with strong participation of Fe(II) empty d-orbitals, which leads to a large CB dispersion and a *ca.* 1 eV bandgap reduction compared to the low-spin state.

The computed band structure for **P2** shows small dispersion in the valence band (Fig. 4), with predicted m_h^* values of 2.20 and 2.34 m_0 through $-(Fe-N-N-)_\infty$ and ligand directions, respectively (Table 1). Similarly, the conduction band is mostly flat, with m_e^* of 2.92 m_0 along the ligands and larger than 10 m_0 for the Fe–N chain direction. DOS shows that the major contribution to the VB comes from the Fe(II) atoms along with the BDT ligand, whereas the CB is fully described by the BDT atoms (Fig. S3). The frontier crystal orbital corresponding to the VBM is calculated to be localized on the inorganic cluster (Fe(II) atoms) and expands to the electron-donor deprotonated BDT^{2-} ligands (Fig. 4). On the other hand, the CBM is found to be localized over the half-protonated $HBDT^-$ ligands only. Due to the random distribution of the protonated ligands, the electronic communication pathways are broken in this polymorph, hence leading to strong localization of the polaron and large m_h^* and m_e^* values. These results suggest that **P2** is expected to be a poor conductor for both holes and electrons.

Finally, the electronic band structure computed for the record conducting 3D MOF **P3** reveals high dispersion in both the valence and conduction band levels (Fig. 4). Small hole effective masses (m_h^*) of 0.36 and 1.40 m_0 are calculated through BDT^{2-} and $-(Fe-N-N-)_\infty$ directions, respectively (Table 1). On the other hand, the conduction band provides a small electron effective mass (m_e^*) of 0.74 m_0 through H_2BDT ligands, whereas large values ($>10\ m_0$) are calculated along the remaining directions. Analogously to **P2**, the density of states calculated for **P3** indicates the involvement of both Fe(II) and BDT atoms (C and N) in the VB, while only ligand atoms contribute to the CB (Fig. S3). Representation of the frontier crystal orbital of the VBM in **P3** shows a complete delocalization over the electron-donor BDT^{2-} ligands (*c* direction) and through the $-(Fe-N-N-)_\infty$ chain (Fig. 4). On the other hand, the CBM is delocalized over the fully protonated H_2BDT ligands, which have a strong electron-accepting character. These results indicate that polymorph **P3** can conduct both electrons and holes efficiently (effective masses $<1\ m_0$), thus presenting ambipolar semiconductivity in orthogonal directions: holes along *c* (BDT^{2-}) and electrons along *b* (H_2BDT).

Notably, the deprotonated BDT^{2-} ligands in **P3** are geometrically bent (maximum curvature depth of 1 Å, Fig. 2), which may impact on the electronic properties of the MOF compared to its polymorphic analogues; in particular, the nature and position of the valence band. Molecular-level analysis of the BDT^{2-} scaffold in its flat (minimum-energy geometry) and curved (as extracted from the **P3** crystal structure) conformations was performed at the HSE06/tier-1 NAO level. The curved BDT^{2-} ligand has a HOMO level 0.12 eV higher in energy compared to the flat structure, while keeping the same orbital topology (Fig. S4). Additionally, as predicted in the molecular calculations of the different protonation states of BDT (*vide supra*), the LUMO in

fully protonated H_2BDT is placed lower in energy compared to partially deprotonated $HBDT^-$, due to its stronger electron-accepting character. The combination of these two factors leads **P3** to present the smallest bandgap value (1.94 eV) among the $Fe_2(BDT)_3$ family of MOFs, a beneficial characteristic to boost conductivity through generation of charge carriers by means of VB → CB electronic transitions.

Protonation distribution

As the proton distribution in BDT ligands impacts the electronic properties of $Fe_2(BDT)_3$ polymorphs, we carried out an analysis of the effect of altering the natural protonic positions on those properties. For simplicity, we centred our comparison on the extreme situations: directions with full protonated or full deprotonated ligands, and fully random protonation. We modelled **P2**, which naturally presents a random protonation, in an ordered protonic distribution (**P2′**), and **P3**, which is naturally ordered, in a random protonic distribution (**P3′**). The chemical formula is maintained to be $Fe_2(H_{0.67}BDT)_3$ in each case. The band structure predicted for the random distribution **P3′** (Fig. S5) indicates significant differences with respect to ordered **P3** (Fig. 4): there is a reduced dispersion of the energy levels around the bandgap region, together with a notable increase in the bandgap from 1.94 eV in **P3** to 2.53 eV in **P3′**, stemming from the absence of strong electron-accepting H_2BDT units in the latter. The smallest predicted effective masses in **P3′** for hole and electron are 0.69 and 2.96 m_0, respectively, compared to 0.36 and 0.67 m_0 in **P3**, which points towards a hindered charge transport of both charge carriers upon random protonic distribution. This result is confirmed by analyzing the topological representation of the frontier VBM and CBM crystal orbitals in **P3′**, which are strongly localized over the deprotonated and protonated tetrazole rings, respectively (Fig. 5). A large energy penalty of 0.57 eV f.u.$^{-1}$ is predicted to promote random protonation from **P3** to **P3′**.

More interesting is the case of the ordered protonic distribution modelled in **P2′** polymorph, which results in a highly dispersive band structure (Fig. S5), together with a smaller bandgap (1.94 eV), compared to randomly protonated **P2** (2.27 eV). In fact, the bandgap calculated for ordered **P2′** is identical to that predicted for record conducting **P3** due to the presence of fully protonated (H_2BDT) and deprotonated (BDT^{2-}) ligands. The computed effective masses for the VB in **P2′** are significantly smaller than those predicted for **P2**, especially along the BDT^{2-} direction (m_h^* from 2.34 m_0 in **P2** to 0.61 m_0 in **P2′**, Table 1). Similarly, the effective mass values obtained for CBM are notoriously reduced for the protonically ordered **P2′**, leading to the smallest m_e^* among all the polymorphs (0.50 m_0 in the H_2BDT direction, Table 1). The frontier crystalline orbitals for the VBM and CBM of **P2′** are fully delocalized over the electron-donating BDT^{2-} and electron-accepting H_2BDT directions (Fig. 5), respectively, thus providing further evidence of a more effective carrier delocalization, a requirement for an efficient charge transport. **P2′** is calculated only 0.02 eV f.u.$^{-1}$ higher in energy than **P2**, indicating that the protonic ordering in this polymorph is energetically accessible,

19032 | *J. Mater. Chem. C*, 2025, **13**, 19026–19036

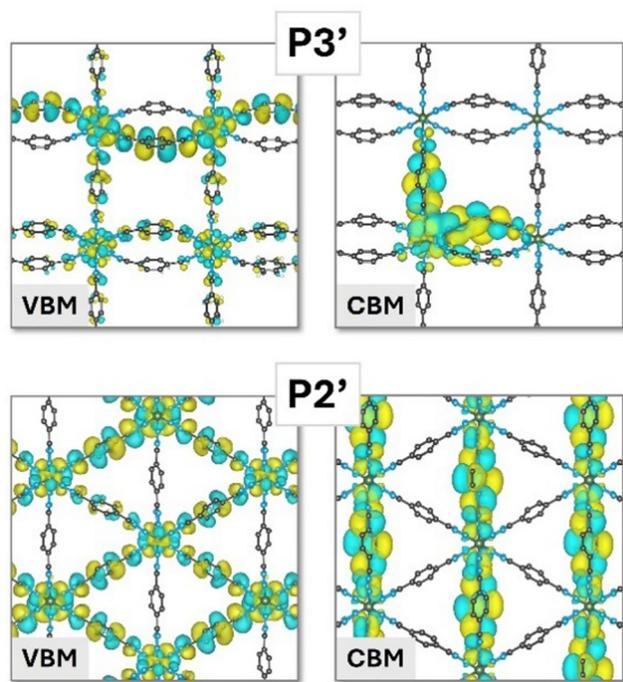This journal is © The Royal Society of Chemistry 2025

Fig. 5 Valence-band maximum (VBM) and conduction-band maximum (CBM) crystal orbitals calculated at the HSE06/tier-1 intermediate NAO level of theory for **P3′** (random protonation distribution) and **P2′** (ordered protonation distribution). In the case of **P3′**, a $1 \times 1 \times 2$ supercell was modelled to allow for a random protonic distribution.

thus constituting a promising new strategy to enhance charge conduction in MOFs.

Oxidation and mixed valence

$Fe_2(BDT)_3$ polymorph **P3** is demonstrated experimentally to show a mixed-valence character upon exposure to atmospheric air. There is an increase in conductivity from 10^{-5} S cm^{-1} (just after synthesis), to 0.3 S cm^{-1} (after 7 days), to 1.2 S cm^{-1} (after 30 days), and to a record maximum conductivity of 1.8 S cm^{-1}, which suggests that charge carrier generation occurs spontaneously through oxidation of Fe(II) to Fe(III).[36] To shed light on

this oxidation phenomenon, we modelled polymorphs **P1**, **P2** and **P3** with 50% of Fe(II) and 50% of Fe(III). Depending on the crystal-field splitting caused by the BDT ligands, the electronic configuration of Fe(III) can be described by either five unpaired electrons (HS configuration) or one unpaired electron (LS configuration). The most stable configuration for the mixed-valence $Fe_2(BDT)_3$ polymorphs is the one where both the Fe(II) and Fe(III) atoms are in their LS configuration for **P2** and **P3**, while for **P1** the Fe(II)(HS)–Fe(III)(HS) configuration is the most favoured configuration (Table S4). Polymorphs were also modelled with a singly oxidized Fe(III) atom to estimate the energy penalty required to ionize the material. The ionization potential (IP) values predicted at the HSE06 level are relatively small for all the polymorphs: 7.25, 6.73 and 6.98 eV for **P1**, **P2** and **P3**, respectively. The smaller IP calculated for **P2** compared to **P1** and **P3** stems from the localized nature of the highest-occupied crystal orbital promoted by the presence of isolated BDT^{2-} units. Note that the IP of referable electron-donating tetrathiafulvalene unit is 6.92 eV,[57] thus highlighting the ability of $Fe_2(BDT)_3$ materials to be easily oxidized and promote mixed-valence processes.

The electronic band structure of mixed-valence Fe(II/III) **P3** (Fig. 6a) is predicted with a direct bandgap of 1.16 eV at Γ, significantly smaller than that obtained for Fe(II)-based **P3** (1.94 eV). This reduction is attributed to the insertion of unoccupied Fe(III) d-electronic levels within the bandgap upon oxidation of iron atoms (Fig. 6a).[36] The topological representation of the β-channel frontier crystalline orbitals supports this statement, as the CBM corresponds to the unoccupied Fe(III) d-orbitals (Fig. 6b), which is further confirmed by the density of states (Fig. 6a) and the spin density (unpaired electrons in the Fe(III) atoms; Fig. S6). In this case, the VBM is centred over the BDT^{2-} ligands with a residual participation of iron atoms (Fig. 6b). Similarly, we modelled the mixed-valence crystals for **P1** and **P2**, yielding analogous results to those obtained for **P3** (Fig. S7 and S8): due to the presence of low-lying Fe(III) empty d-levels in the mixed-valence system, a significant bandgap reduction is predicted from 2.18 to 0.38 eV in **P1** and from 2.27 to 0.96 eV in **P2**. However, unlike mixed-valence **P2** and **P3**,
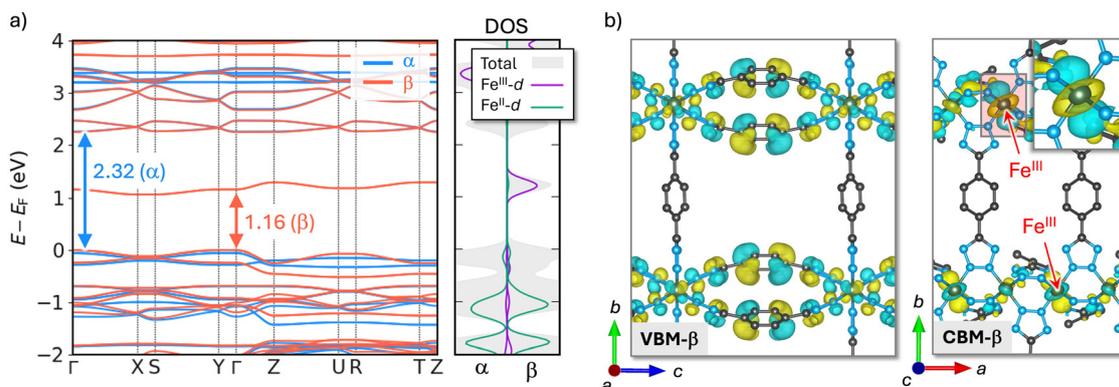

Fig. 6 (a) Band structure and DOS calculated at the HSE06 level of theory for mixed-valence **P3** with both Fe(II) and Fe(III) in LS configuration. The Fermi level is set to zero at the top of valence band. (b) VBM and CBM crystal orbitals (β channel) of mixed-valence **P3**. The topology of CBM-β on one of the Fe(III) atoms is shown in the inset.

This journal is © The Royal Society of Chemistry 2025

J. Mater. Chem. C, 2025, **13**, 19026–19036 | **19033**

both β-channel VBM and CBM of **P1** correspond to the Fe(III) d-orbitals. As exemplified in the band structure of mixed-valence **P3** (Fig. 6), the frontier energy levels maintain large dispersion, with effective masses as small as $m_h^* = 0.51\,m_0$ and $m_e^* = 0.67\,m_0$ through Γ–Z direction, whereas a moderate electron transport $\left(m_e^* = 2.91\,m_0\right)$ is calculated through Γ–X Fe–N chain direction.

Conclusions

The conducting properties of three different polymorphs (**P1–3**) of a 3D Fe(II)-based metal–organic framework with tetrazole BDT ligands, $Fe_2(BDT)_3$, have been investigated using density functional theory. In addition to the $-(Fe-N-N-)_\infty$ building block chain, alternative routes based on the BDT ligand define efficient charge-transport channels in these materials. The proton distribution along the organic ligands is key to understanding the bandgap trends and the extent of the polaron delocalization along the framework, ultimately defining different charge-transport pathways for each polymorph. In particular, polymorph **P3** with an orthogonal arrangement of fully protonated H_2BDT and fully deprotonated BDT^{2-} ligands, provides the smallest bandgap as well as the smallest hole and electron effective masses among the series, thus standing as a promising ambipolar conductor. In contrast, polymorph **P2** displays a random distribution of protonation, which leads to a strong localization of the electronic structure and large carrier effective masses (poor conductivity). Protonic ordering is presented as a new strategy in the **P2** framework to boost the electronic properties of the material, reducing the bandgap in 0.3 eV and lowering the hole and electron effective masses down to half the free electron mass. Finally, we demonstrate that partial oxidation of the porous frameworks is energetically comparable to prototypical organic electron donors. Modelling of the corresponding mixed-valence Fe(II)/Fe(III) $Fe_2(BDT)_3$ materials confirms the insertion of empty Fe(III)-d energy levels within the band edges for the three polymorphs, thus reducing the bandgap values under 1 eV and facilitating charge carrier generation through valence band to conduction band electronic transitions.

Author contributions

M. E.-R. and J. F.-G. performed all theoretical calculations. M. E.-R. and J. C. wrote the manuscript. E. O., A. W. and J. C. revised the theoretical analysis and the manuscript.

Conflicts of interest

There are no conflicts to declare.

Data availability

Additional benchmark data, figures, tables and computational details are included in the SI. See DOI: https://doi.org/10.1039/d5tc02135a

Acknowledgements

References

1 M. Dincă and J. R. Long, Introduction: Porous Framework Chemistry, *Chem. Rev.*, 2020, **120**(16), 8037–8038, DOI: 10.1021/acs.chemrev.0c00836.

2 B. F. Hoskins and R. Robson, Infinite Polymeric Frameworks Consisting of Three Dimensionally Linked Rod-like Segments, *J. Am. Chem. Soc.*, 1989, **111**(15), 5962–5964, DOI: 10.1021/ja00197a079.

3 O. M. Yaghi, G. Li and H. Li, Selective Binding and Removal of Guests in a Microporous Metal–Organic Framework, *Nature*, 1995, **378**(6558), 703–706, DOI: 10.1038/378703a0.

4 G. M. Espallargas and E. Coronado, Magnetic Functionalities in MOFs: From the Framework to the Pore, *Chem. Soc. Rev.*, 2018, **47**(2), 533–557, DOI: 10.1039/C7CS00653E.

5 S. M. J. Rogge, A. Bavykina, J. Hajek, H. Garcia, A. I. Olivos-Suarez, A. Sepúlveda-Escribano, A. Vimont, G. Clet, P. Bazin, F. Kapteijn, M. Daturi, E. V. Ramos-Fernandez, F. X. L. i Xamena, V. V. Speybroeck and J. Gascon, Metal–Organic and Covalent Organic Frameworks as Single-Site Catalysts, *Chem. Soc. Rev.*, 2017, **46**(11), 3134–3184, DOI: 10.1039/C7CS00033B.

6 K. Sumida, D. L. Rogow, J. A. Mason, T. M. McDonald, E. D. Bloch, Z. R. Herm, T.-H. Bae and J. R. Long, Carbon Dioxide Capture in Metal–Organic Frameworks, *Chem. Rev.*, 2012, **112**(2), 724–781, DOI: 10.1021/cr2003272.

7 M. D. Allendorf, R. Dong, X. Feng, S. Kaskel, D. Matoga and V. Stavila, Electronic Devices Using Open Framework Materials, *Chem. Rev.*, 2020, **120**(16), 8581–8640, DOI: 10.1021/acs.chemrev.0c00033.

8 M. Souto, K. Strutyński, M. Melle-Franco and J. Rocha, Electroactive Organic Building Blocks for the Chemical Design of Functional Porous Frameworks (MOFs and COFs) in Electronics, *Chem. – Eur. J.*, 2020, **26**(48), 10912–10935, DOI: 10.1002/chem.202001211.

9 M. Vicent-Morales, M. Esteve-Rochina, J. Calbo, E. Ortí, I. J. Vitórica-Yrezábal and G. Mínguez Espallargas, Semiconductor Porous Hydrogen-Bonded Organic Frameworks Based on Tetrathiafulvalene Derivatives, *J. Am. Chem. Soc.*, 2022, **144**(20), 9074–9082, DOI: 10.1021/jacs.2c01957.

10 T. C. Narayan, T. Miyakai, S. Seki and M. Dincă, High Charge Mobility in a Tetrathiafulvalene-Based Microporous Metal–Organic Framework, *J. Am. Chem. Soc.*, 2012, **134**(31), 12932–12935, DOI: 10.1021/ja3059827.

19034 | *J. Mater. Chem. C*, 2025, **13**, 19026–19036

This journal is © The Royal Society of Chemistry 2025

11 M. Souto, A. Santiago-Portillo, M. Palomino, I. J. Vitórica-Yrezábal, B. J. C. Vieira, J. C. Waerenborgh, S. Valencia, S. Navalón, F. Rey, H. García and G. M. Espallargas, A Highly Stable and Hierarchical Tetrathiafulvalene-Based Metal–Organic Framework with Improved Performance as a Solid Catalyst, *Chem. Sci.*, 2018, **9**(9), 2413–2418, DOI: **10.1039/C7SC04829G**.

12 G. Valente, M. Esteve-Rochina, A. Paracana, A. Rodríguez-Diéguez, D. Choquesillo-Lazarte, E. Ortí, J. Calbo, M. Ilkaeva, L. Mafra, M. A. Hernández-Rodríguez, J. Rocha, H. Alves and M. Souto, Through-Space Hopping Transport in an Iodine-Doped Perylene-Based Metal–Organic Framework, *Mol. Syst. Des. Eng.*, 2022, **7**(9), 1065–1072, DOI: **10.1039/D2ME00108J**.

13 J. M. Seco, E. San Sebastián, J. Cepeda, B. Biel, A. Salinas-Castillo, B. Fernández, D. P. Morales, M. Bobinger, S. Gómez-Ruiz, F. C. Loghin, A. Rivadeneyra and A. Rodríguez-Diéguez, A Potassium Metal-Organic Framework Based on Perylene-3,4,9,10-Tetracarboxylate as Sensing Layer for Humidity Actuators, *Sci. Rep.*, 2018, **8**(1), 14414, DOI: **10.1038/s41598-018-32810-7**.

14 F. Mo, Q. Han, M. Chen, H. Meng, J. Guo and Y. Fu, Novel Optoelectronic Metal Organic Framework Material Perylene Tetracarboxylate Magnesium: Preparation and Biosensing, *Nanoscale*, 2021, **13**(38), 16244–16250, DOI: **10.1039/D1NR03300J**.

15 J.-H. Deng, X.-L. Yuan and G.-Q. Mei, A Three-Dimensional Highly Stable Zn(II) Coordination Polymer Based on 1,4-Benzeneditetrazolate (H2BDT): Synthesis, Crystal Structure, and Luminescent Properties, *Inorg. Chem. Commun.*, 2010, **13**(12), 1585–1589, DOI: **10.1016/j.inoche.2010.09.023**.

16 M. Dincă, A. F. Yu and J. R. Long, Microporous Metal−Organic Frameworks Incorporating 1,4-Benzeneditetrazolate: Syntheses, Structures, and Hydrogen Storage Properties, *J. Am. Chem. Soc.*, 2006, **128**(27), 8904–8913, DOI: **10.1021/ja061716i**.

17 M.-H. Zeng, Q.-X. Wang, Y.-X. Tan, S. Hu, H.-X. Zhao, L.-S. Long and M. Kurmoo, Rigid Pillars and Double Walls in a Porous Metal-Organic Framework: Single-Crystal to Single-Crystal, Controlled Uptake and Release of Iodine and Electrical Conductivity, *J. Am. Chem. Soc.*, 2010, **132**(8), 2561–2563, DOI: **10.1021/ja908293n**.

18 Z. Yin, Q.-X. Wang and M.-H. Zeng, Iodine Release and Recovery, Influence of Polyiodide Anions on Electrical Conductivity and Nonlinear Optical Activity in an Interdigitated and Interpenetrated Bipillared-Bilayer Metal–Organic Framework, *J. Am. Chem. Soc.*, 2012, **134**(10), 4857–4863, DOI: **10.1021/ja211381e**.

19 H.-Y. Wang, J.-Y. Ge, C. Hua, C.-Q. Jiao, Y. Wu, C. F. Leong, D. M. D'Alessandro, T. Liu and J.-L. Zuo, Photo- and Electronically Switchable Spin-Crossover Iron(II) Metal–Organic Frameworks Based on a Tetrathiafulvalene Ligand, *Angew. Chem. Int. Ed.*, 2017, **56**(20), 5465–5470, DOI: **10.1002/anie.201611824**.

20 J. Su, S. Yuan, H.-Y. Wang, L. Huang, J.-Y. Ge, E. Joseph, J. Qin, T. Cagin, J.-L. Zuo and H.-C. Zhou, Redox-Switchable Breathing Behavior in Tetrathiafulvalene-Based Metal–Organic Frameworks, *Nat. Commun.*, 2017, **8**(1), 2008, DOI: **10.1038/s41467-017-02256-y**.

21 A. A. Talin, A. Centrone, A. C. Ford, M. E. Foster, V. Stavila, P. Haney, R. A. Kinney, V. Szalai, F. El Gabaly, H. P. Yoon, F. Léonard and M. D. Allendorf, Tunable Electrical Conductivity in Metal-Organic Framework Thin-Film Devices, *Science*, 2014, **343**(6166), 66–69, DOI: **10.1126/science.1246738**.

22 M. Bláha, V. Valeš, Z. Bastl, M. Kalbáč and H. Shiozawa, Host–Guest Interactions in Metal–Organic Frameworks Doped with Acceptor Molecules as Revealed by Resonance Raman Spectroscopy, *J. Phys. Chem. C*, 2020, **124**(44), 24245–24250, DOI: **10.1021/acs.jpcc.0c07473**.

23 M. D. Allendorf, M. E. Foster, F. Léonard, V. Stavila, P. L. Feng, F. P. Doty, K. Leong, E. Y. Ma, S. R. Johnston and A. A. Talin, Guest-Induced Emergent Properties in Metal–Organic Frameworks, *J. Phys. Chem. Lett.*, 2015, **6**(7), 1182–1195, DOI: **10.1021/jz5026883**.

24 T. T. Debela and C. H. Hendon, Hydrogenic Defects in Ferromagnetic Cu3(HITP)2 (HITP ≡ 2,3,6,7,10,11-Hexaimino-triphenylene), a 2D Metal–Organic Framework, *ACS Mater. Lett.*, 2024, **6**(7), 2698–2702, DOI: **10.1021/acsmaterials lett.4c00923**.

25 G. Xu, C. Zhu and G. Gao, Recent Progress of Advanced Conductive Metal–Organic Frameworks: Precise Synthesis, Electrochemical Energy Storage Applications, and Future Challenges, *Small*, 2022, **18**(44), 2203140, DOI: **10.1002/smll.202203140**.

26 R. Dong, P. Han, H. Arora, M. Ballabio, M. Karakus, Z. Zhang, C. Shekhar, P. Adler, P. S. Petkov, A. Erbe, S. C. B. Mannsfeld, C. Felser, T. Heine, M. Bonn, X. Feng and E. Cánovas, High-Mobility Band-like Charge Transport in a Semiconducting Two-Dimensional Metal–Organic Framework, *Nat. Mater.*, 2018, **17**(11), 1027–1032, DOI: **10.1038/s41563-018-0189-z**.

27 X. Huang, P. Sheng, Z. Tu, F. Zhang, J. Wang, H. Geng, Y. Zou, C. Di, Y. Yi, Y. Sun, W. Xu and D. Zhu, A Two-Dimensional π–d Conjugated Coordination Polymer with Extremely High Electrical Conductivity and Ambipolar Transport Behaviour, *Nat. Commun.*, 2015, **6**(1), 7408, DOI: **10.1038/ncomms8408**.

28 J. G. Park, M. L. Aubrey, J. Oktawiec, K. Chakarawet, L. E. Darago, F. Grandjean, G. J. Long and J. R. Long, Charge Delocalization and Bulk Electronic Conductivity in the Mixed-Valence Metal–Organic Framework Fe(1,2,3-Triazolate)2(BF4)x, *J. Am. Chem. Soc.*, 2018, **140**(27), 8526–8534, DOI: **10.1021/jacs.8b03696**.

29 S. Li, Y. Wang, C. Qi, X. Zhao, J. Zhang and S. Zhang, 3D Energetic Metal–Organic Frameworks: Synthesis and Properties of High Energy Materials, *Angew. Chem., Int. Ed.*, 2013, **52**(52), 14031–14035, DOI: **10.1002/anie.201307118**.

30 L. Sun, C. H. Hendon, S. S. Park, Y. Tulchinsky, R. Wan, F. Wang, A. Walsh and M. Dincă, Is Iron Unique in Promoting Electrical Conductivity in MOFs?, *Chem. Sci.*, 2017, **8**(6), 4450–4457, DOI: **10.1039/C7SC00647K**.

31 Z. Yan, M. Li, H.-L. Gao, X.-C. Huang and D. Li, High-Spin versus Spin-Crossover versus Low-Spin: Geometry Intervention in Cooperativity in a 3D Polymorphic Iron(II)–Tetrazole MOFs System, *Chem. Commun.*, 2012, **48**(33), 3960–3962, DOI: **10.1039/C2CC18140A**.

This journal is © The Royal Society of Chemistry 2025

J. Mater. Chem. C, 2025, **13**, 19026–19036 | **19035**

32 W.-T. Liu, J.-Y. Li, J.-P. Ni, X. Bao, Y.-C. Ou, J.-D. Leng, J.-L. Liu and M.-L. Tong, Incomplete Spin Crossover versus Antiferromagnetic Behavior Exhibited in Three-Dimensional Porous Fe(II)-Bis(Tetrazolate) Frameworks, *Cryst. Growth Des.*, 2012, **12**(3), 1482–1488, DOI: **10.1021/cg201569m**.

33 M. A. Halcrow, Structure:Function Relationships in Molecular Spin-Crossover Complexes, *Chem. Soc. Rev.*, 2011, **40**(7), 4119–4142, DOI: **10.1039/C1CS15046D**.

34 J. Krober, E. Codjovi, O. Kahn, F. Groliere and C. Jay, A Spin Transition System with a Thermal Hysteresis at Room Temperature, *J. Am. Chem. Soc.*, 1993, **115**(21), 9810–9811, DOI: **10.1021/ja00074a062**.

35 J. Tao, R.-J. Wei, R.-B. Huang and L.-S. Zheng, Polymorphism in Spin-Crossover Systems, *Chem. Soc. Rev.*, 2012, **41**(2), 703–737, DOI: **10.1039/C1CS15136C**.

36 L. S. Xie, L. Sun, R. Wan, S. S. Park, J. A. DeGayner, C. H. Hendon and M. Dincă, Tunable Mixed-Valence Doping toward Record Electrical Conductivity in a Three-Dimensional Metal–Organic Framework, *J. Am. Chem. Soc.*, 2018, **140**(24), 7411–7414, DOI: **10.1021/jacs.8b03604**.

37 S. Bonnet, M. A. Siegler, J. S. Costa, G. Molnár, A. Bousseksou, A. L. Spek, P. Gamez and J. Reedijk, A Two-Step Spin Crossover Mononuclear Iron(II) Complex with a [HS–LS–LS] Intermediate Phase, *Chem. Commun.*, 2008, 5619–5621, DOI: **10.1039/B811746B**.

38 V. Blum, R. Gehrke, F. Hanke, P. Havu, V. Havu, X. Ren, K. Reuter and M. Scheffler, Ab Initio Molecular Simulations with Numeric Atom-Centered Orbitals, *Comput. Phys. Commun.*, 2009, **180**(11), 2175–2196, DOI: **10.1016/j.cpc.2009.06.022**.

39 V. Havu, V. Blum, P. Havu and M. Scheffler, Efficient O(N) Integration for All-Electron Electronic Structure Calculation Using Numeric Basis Functions, *J. Comput. Phys.*, 2009, **228**(22), 8367–8379, DOI: **10.1016/j.jcp.2009.08.008**.

40 X. Ren, P. Rinke, V. Blum, J. Wieferink, A. Tkatchenko, A. Sanfilippo, K. Reuter and M. Scheffler, Resolution-of-Identity Approach to Hartree–Fock, Haybrid Density Functionals, RPA, MP2 and GW with Numeric Atom-Centered Orbital Basis Functions, *New J. Phys.*, 2012, **14**(5), 053020, DOI: **10.1088/1367-2630/14/5/053020**.

41 J. Nocedal and S. J. Wright, *Numerical Optimization*, Springer series in operations research, Springer, New York, 1999.

42 J. P. Perdew, A. Ruzsinszky, G. I. Csonka, O. A. Vydrov, G. E. Scuseria, L. A. Constantin, X. Zhou and K. Burke, Restoring the Density-Gradient Expansion for Exchange in Solids and Surfaces, *Phys. Rev. Lett.*, 2008, **100**(13), 136406, DOI: **10.1103/PhysRevLett.100.136406**.

43 A. V. Krukau, O. A. Vydrov, A. F. Izmaylov and G. E. Scuseria, Influence of the Exchange Screening Parameter on the Performance of Screened Hybrid Functionals, *J. Chem. Phys.*, 2006, **125**(22), 224106, DOI: **10.1063/1.2404663**.

44 E. van Lenthe, J. G. Snijders and E. J. Baerends, The Zero-order Regular Approximation for Relativistic Effects: The Effect of Spin–Orbit Coupling in Closed Shell Molecules, *J. Chem. Phys.*, 1996, **105**(15), 6505–6516, DOI: **10.1063/1.472460**.

45 P. Verma and D. G. Truhlar, Does DFT+U Mimic Hybrid Density Functionals?, *Theor. Chem. Acc.*, 2016, **135**(8), 182, DOI: **10.1007/s00214-016-1927-4**.

46 K. T. Butler, C. H. Hendon and A. Walsh, Electronic Chemical Potentials of Porous Metal–Organic Frameworks, *J. Am. Chem. Soc.*, 2014, **136**(7), 2703–2706, DOI: **10.1021/ja4110073**.

47 L. D. Whalley, J. M. Frost, B. J. Morgan and A. Walsh, Impact of Nonparabolic Electronic Band Structure on the Optical and Transport Properties of Photovoltaic Materials, *Phys. Rev. B*, 2019, **99**(8), 085207, DOI: **10.1103/PhysRevB.99.085207**.

48 L. D. Whalley, Effmass: An Effective Mass Package, *J. Open Source Softw.*, 2018, **3**(28), 797, DOI: **10.21105/joss.00797**.

49 K. Momma and F. Izumi, VESTA 3 for Three-Dimensional Visualization of Crystal, Volumetric and Morphology Data, *J. Appl. Cryst.*, 2011, **44**(6), 1272–1276, DOI: **10.1107/S0021889811038970**.

50 *Chemcraft – Citation*. **https://www.chemcraftprog.com/citation.html** (accessed 2024-07-24).

51 T. Koopmans, Über Die Zuordnung von Wellenfunktionen Und Eigenwerten Zu Den Einzelnen Elektronen Eines Atoms, *Physica*, 1934, **1**(1), 104–113, DOI: **10.1016/S0031-8914(34)90011-2**.

52 G. Prokopiou and L. Kronik, Spin-State Energetics of Fe Complexes from an Optimally Tuned Range-Separated Hybrid Functional, *Chem. – Eur. J.*, 2018, **24**(20), 5173–5182, DOI: **10.1002/chem.201704014**.

53 L. A. Mariano, B. Vlaisavljevich and R. Poloni, Biased Spin-State Energetics of Fe(II) Molecular Complexes within Density-Functional Theory and the Linear-Response Hubbard U Correction, *J. Chem. Theory Comput.*, 2020, **16**(11), 6755–6762, DOI: **10.1021/acs.jctc.0c00628**.

54 L. A. Mariano, B. Vlaisavljevich and R. Poloni, Improved Spin-State Energy Differences of Fe(II) Molecular and Crystalline Complexes via the Hubbard U-Corrected Density, *J. Chem. Theory Comput.*, 2021, **17**(5), 2807–2816, DOI: **10.1021/acs.jctc.1c00034**.

55 M. G. Taylor, T. Yang, S. Lin, A. Nandy, J. P. Janet, C. Duan and H. J. Kulik, Seeing Is Believing: Experimental Spin States from Machine Learning Model Structure Predictions, *J. Phys. Chem. A*, 2020, **124**(16), 3286–3299, DOI: **10.1021/acs.jpca.0c01458**.

56 A. Tkatchenko and M. Scheffler, Accurate Molecular van der Waals Interactions from Ground-State Electron Density and Free-Atom Reference Data, *Phys. Rev. Lett.*, 2009, **102**(7), 073005, DOI: **10.1103/PhysRevLett.102.073005**.

57 T. Kobayashi, Z. Yoshida, H. Awaji, T. Kawase and S. Yoneda, Intramolecular Orbital Interactions in 6,6′-Bi(1,4-Dithiafulvenyl) Studied by Photoelectron Spectroscopy, *Bull. Chem. Soc. Jpn.*, 1984, **57**(9), 2591–2595, DOI: **10.1246/bcsj.57.2591**.

19036 | *J. Mater. Chem. C*, 2025, **13**, 19026–19036

This journal is © The Royal Society of Chemistry 2025